Progress in the Understanding of Drug–Receptor Interactions, Part 2: Experimental and Theoretical Electrostatic Moments and Interaction Energies of an Angiotensin II Receptor Antagonist ($C_{30}H_{30}N_6O_3S$)

Raffaella Soave,[a] **Mario Barzaghi,**[a] **and Riccardo Destro**[b]

Abstract: A combined experimental and theoretical charge density study of an angiotensin II receptor antagonist (**1**) is presented focusing on electrostatic properties such as atomic charges, molecular electric moments up to the fourth rank and energies of the intermolecular interactions, to gain an insight into the physical nature of the drug–receptor interaction. Electrostatic properties were derived from both the experimental electron density (multipole refinement of X-ray data collected at $T = 17$ K) and the ab initio wavefunction (single molecule and fully periodic calculations at the DFT level). The relevance of S⋯O and S⋯N intramolecular interactions on the activity of **1** is highlighted by using both the crystal and gas-phase geometries and their electrostatic nature is documented by means of QTAIM atomic charges. The derived electrostatic properties are consistent with a nearly spherical electron density distribution, characterised by an intermingling of electropositive and -negative zones rather than by a unique electrophilic region opposed to a nucleophilic area. This makes the first molecular moment scarcely significant and ill-determined, whereas the second moment is large, significant and highly reliable. A comparison between experimental and theoretical components of the third electric moment shows a few discrepancies, whereas the agreement for the fourth electric moment is excellent. The most favourable intermolecular bond is show to be an NH⋯N hydrogen bond with an energy of about 50 kJ mol^{-1}. Key pharmacophoric features responsible for attractive electrostatic interactions include CH⋯X hydrogen bonds. It is shown that methyl and methylene groups, known to be essential for the biological activity of the drug, provide a significant energetic contribution to the total binding energy. Dispersive interactions are important at the thiophene and at both the phenyl fragments. The experimental estimates of the electrostatic contribution to the intermolecular interaction energies of six molecular pairs, obtained by a new model proposed by Spackman, predict the correct relative electrostatic energies with no exceptions.

Keywords: angiotensin II · charge density distribution · electric moments · electrostatic interactions · molecular recognition

Introduction

In the last decade several attempts have been made to understand the molecular basis for hypertension through the study of sartans, a class of non-peptide angiotensin II (AII) antagonists: the structural features that characterise the pharmacophoric fragments of these drugs have been widely examined, the final target being the prediction of the drug–receptor interaction.[1–4] As for most drugs and hormones, the physiological effect of sartans is accomplished by binding to a specific receptor, the AT_1 receptor: according to the "lock and key" model, frequently adopted in molecular modelling calculations, it is assumed that the receptor has specific steric requirements that enable recognition of only the natural substrate and closely related analogues. This is the basis of the structure–activity approach to drug design.

In addition to steric interactions, another important prerequisite for binding is a high degree of complementarity between the charge distributions of the drug and its receptor. A detailed description of the total charge density and of the electrostatic properties (such as the electrostatic poten-

[a] Dr. R. Soave, Dr. M. Barzaghi
CNR-ISTM, Istituto di Scienze e Tecnologie Molecolari
Via Golgi 19, 20133 Milano (Italy)
Fax: (+39) 02-503-14300
E-mail: raffaella.soave@istm.cnr.it

[b] Prof. R. Destro
Dipartimento di Chimica Fisica e Elettrochimica
Universita' di Milano e CNR-ISTM
Via Golgi 19, 20133 Milano (Italy)

tial and the electric moments) of the drug is crucial to quantify the energy of interaction with the receptor[5–7] and to characterise the key features of its biological activity, with special reference to selectivity and specificity of binding. However, while the electrostatic potential is now widely acknowledged as a reactivity index[8,9] and is frequently reported in the literature relating to drug molecules, including some sartans,[1,3] the relevance of first and second electrostatic moments in predicting the binding mechanism in molecular recognition processes has been discussed in only a few cases[10–13] and never in the case of AII antagonists. Electric moments have the great advantage of being derivable with great accuracy from both theoretical calculations and X-ray diffraction experiments of charge density quality:[9,14] a comparison between the two estimates can reveal fundamental insights, for example, into the charge rearrangement that occurs upon crystallisation, and shows benefits and drawbacks of both methods.

We recently reported the low-temperature ($T = 17$ K) X-ray crystal structure of an AT_1-selective angiotensin II receptor antagonist belonging to the class of sartans, named LR-B/081 (alias milfasartan (**1**), see Scheme 1).[15] In that
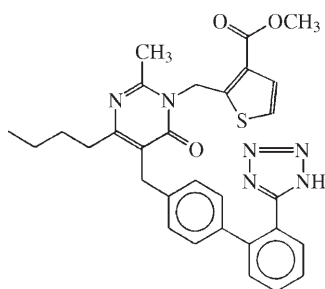
1

Scheme 1. AT_1-selective angiotensin II receptor antagonist LR-B/081.

paper, hereinafter referred to as Paper 1, the structural features of **1** were thoroughly discussed and both the full topological analysis of its experimental charge density distribution $\rho(r)$ and the molecular electrostatic potential $\phi(r)$ were presented. This allowed us to clarify important features of intra- and intermolecular interactions, such as the electrostatic nature of two short S···O and S···N intramolecular contacts that stabilise the overall conformation of **1**, and to elucidate the $\phi(r)$ features which play a key role in the binding to the AII receptor.

The objective of this work was to improve the actual understanding of sartans activity by using the electrostatic moments and the intermolecular interaction energies of milfasartan (obtained from both an X-ray diffraction experiment and the ab initio wavefunction) to characterise the physical nature of the drug–receptor interaction. In particular, reliable answers to the following questions were sought: 1) Which are the key intra- and intermolecular interactions responsible for the high activity of LR-B/081? 2) Is the

nature of the drug–receptor interaction mainly electrostatic or dispersive? 3) Can we gain an insight into the driving force for the recognition process?

Since both the chemical identity and the structure of the AII receptor are unknown,[16] a major limitation of our approach is that the only clues as to the mechanism of drug action are provided by the drug molecules themselves. However, it has recently been acknowledged[17,18] that, as the crystallisation process involves the molecular self-recognition phenomenon, the interactions between nearest neighbours in a molecular crystal closely resemble those between a guest molecule and its host. It follows that the physical properties of a drug molecule such as **1** in its crystal form, explaining the molecular self-affinity that gives rise to crystallisation, can rightly be used as the structural basis for recognising attractive interactions between the drug and its receptor.

In this report several molecular properties of **1** at $T = 17$ K are discussed and compared with the theoretical results obtained for both the crystal and the isolated molecule: 1) geometric and topological features; 2) QTAIM[19] atomic volumes and charges; 3) molecular electric moments up to the fourth rank; 4) hydrogen-bonding properties: energetics and pharmacophoric features; 5) the total intermolecular interaction energy (E_{int}) of dimeric adducts, focusing on the electrostatic contribution (E_{es}) to E_{int}.

Methods

X-ray diffraction: Full crystallographic and refinement details are reported in Paper 1.[15] They can be summarised briefly as follows: a total of 51 485 intensities were collected at $T = 17(1)$ K up to a 2θ value of 75° for graphite-monochromated $Mo_{K\alpha}$ radiation.[20] Weighted averaging of multiple data yielded 14 698 independent reflections of which 13 812 were observed ($I > 0$). The electron density was obtained from the diffraction data by a multipolar expansion up to the hexadecapole level ($l_{max} = 4$) for sulfur, oxygen, nitrogen and carbon atoms and up to the quadrupole level for hydrogen atoms, according to the rigid pseudoatom formalism of Stewart.[21] Anisotropic displacement parameters (ADPs) for hydrogen atoms were also included, as obtained from spectroscopic information and molecular rigid-body librations.[22] All refinements were carried out using the VALRAY[23] program.

CCDC 207037 contains the supplementary crystallographic data for Paper 1. These data can be obtained free of charge from the Cambridge Crystallographic Data Centre via www.ccdc.cam.ac.uk/data_request/cif.

Theoretical calculations: Single-molecule calculations within the framework of the density functional theory (DFT) were performed using the Gaussian 98 (G98)[24] and ADF-2004.01[25,26] programs on the LR-B/081 molecule and on six isolated dimeric adducts using the 17 K experimental geometry. In the G98 calculations, the standard split-valence triple-exponential 6-311G** basis set and Becke's three-parameter hybrid DFT method,[27] combined with the non-local correlation functional of Lee, Yang and Parr (B3LYP)[28] were used, while in the ADF calculations we adopted the standard triple-zeta exponential (TZP) basis set and Becke's 1988 exchange functional[29] combined with Lee, Yang and Parr's correlation functional (BLYP).[28] Geometry optimisation of the LR-B/081 molecule was performed at the B3LYP/6-311G** level of theory using the experimental geometry as an initial guess.

Fully periodic DFT calculations on the 17 K experimental geometry were carried out with the CRYSTAL2003 program[30] using the 6-31G**[31] basis set and the same functional as used in the G98 calculations. Static

structure factors F_c (the same *hkl* indices as in the X-ray experiment) in the range $0 < \sin\theta/\lambda < 0.86$ Å^{-1} were obtained through a Fourier transform of the theoretical periodic $\rho(r)$. Only the charge density multipole parameters (up to the fourth order on sulfur, oxygen, nitrogen and carbon atoms and to the second order on hydrogen atoms, in analogy with the analysis of the experimental structure factors) were varied in the iterative least-squares refinement of F_c using the code VALRAY.[23] In the following and in the tables the notations MCG-B3LYP and MCG-BLYP are used to distinguish molecular calculations on the crystal geometry (with GAUSSIAN and ADF, respectively) from those on the periodic crystal (marked as P-B3LYP), whereas the results of the geometry optimisation are referred to as MOG-B3LYP.

Basis set superposition errors (BSSE) were accounted for by the counterpoise correction method[32] in the calculation of the dimer interaction energies.

Analysis of experimental and theoretical $\rho(r)$ in terms of their topological features, nuclear-centred distributed multipole analyses (DMA) and derived properties were performed by means of the PAMoC (Properties of Atoms and Molecules in molecular Crystals) program,[33] which retrieves all required data from either the binary checkpoint file produced by VALRAY[23] or the AIMPAC wavefunction files[34] generated by G98 and ADF. The topologies of both the theoretical and experimental $\rho(r)$ fulfil the Poincarè Hopf relationship.[19]

Results and Discussion

Geometric and topological features with a comparison between the crystal and gas-phase molecule: The LR-B/081 molecule at 17 K has a molecular structure in the crystal form that roughly fits into a triangle $16 \times 15 \times 14$ Å^3 with the butyl chain, the C22−C23 bond of the 1,6-substituted phenyl group (hereinafter *o*-phenyl group) and the CH$_3$ group of the methyl ester fragment at the three corners of the triangle (Figure 1a). The thiophene, the pyrimidinone and the tetrazole rings are linked in a cyclic structure by three short intramolecular contacts, namely N4···H9 (2.751(6) Å), S1···N5 (3.2950(3) Å) and S1···O1 (3.1995(3) Å), with the associated topological rings (see Paper 1).[15] This structure is further stabilised by the H5A···O3 interaction (2.200(6) Å) which locks the 3-substituted thiophene in a favourable conformation.

Despite the large number of conformational degrees of freedom of this molecule, the gas-phase-optimised molecular conformation (Figure 1b) is similar to that found in the crystal. By comparing the two sets of torsion angles that describe the molecular conformation (Table 1), it can be seen that only a few of them are significantly different, and refer to the relative orientation of the rings in the biphenyltetrazole (BPT) moiety and to the direction of the butyl chain with respect to the central pyrimidinone ring. As in the 17 K experimental structure, the theoretical conformation is characterised by a *syn* orientation of the tetrazole and pyrimidinone rings relative to the 1,4-substituted phenyl ring (hereinafter *p*-phenyl group) and is stabilised by the short intramolecular contacts, N4···H9 (3.3222 Å), S1···N5 (3.2212 Å), S1···O1 (3.3064 Å) and H5A···O3 (2.1992 Å). The experimental and theoretical electron density properties at the bond critical points (bcps) of these interactions are listed in Table 2: it can be seen that, whereas the H5A···O3, S···N
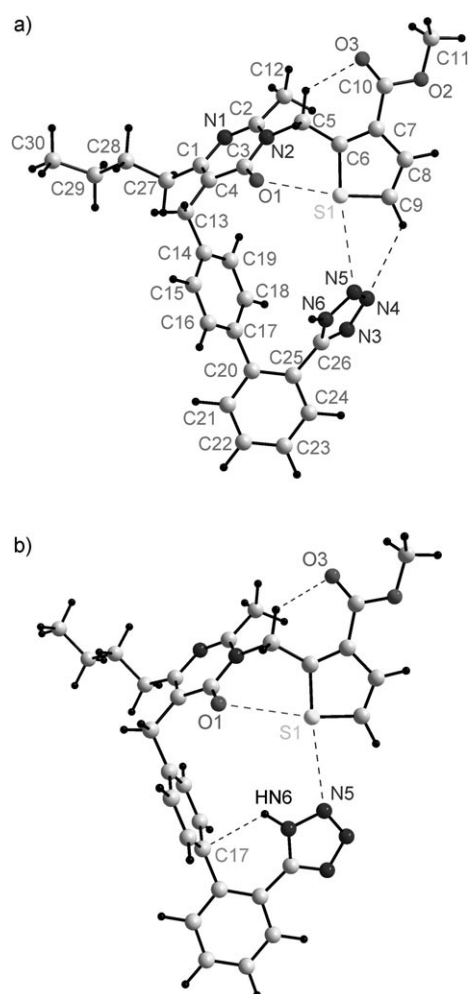

Figure 1. a) Experimentally determined molecular structure of LR-B/081 at 17 K with the atom-numbering scheme. Hydrogen atoms are numbered according to the heavy atom to which they are bonded. b) Gas-phase-optimised molecular conformation of LR-B/081 (MOG-B3LYP). Short intramolecular contacts are represented as dashed lines.

Table 1. Comparison between gas-phase-optimised and experimental (17 K) conformational parameters of LR-B/081.

	Torsion angle [°]	
	MOG-B3LYP	Experimental
$\tau 1 = $ C20-C25-C26-N6	13.89	55.99(5)
$\tau 2 = $ C21-C20-C17-C16	75.79	50.84(4)
$\tau 3 = $ C15-C14-C13-C4	123.16	163.01(2)
$\tau 4 = $ C14-C13-C4-C3	−72.42	−78.25(5)
$\tau 5 = $ C3-N2-C5-C6	94.63	92.44(3)
$\tau 6 = $ N2-C5-C6-C7	128.83	133.33(4)
$\tau 7 = $ C5-C6-C7-C10	−1.17	−3.03(4)
$\tau 8 = $ C6-C7-C10-O2	−181.87	−171.07(3)
$\tau 9 = $ C7-C10-O2-C11	180.16	176.57(3)
$\phi 1 = $ C4-C1-C27-C28	103.56	83.66(4)
$\phi 2 = $ C1-C27-C28-C29	175.72	173.08(2)
$\phi 3 = $ C27-C28-C29-C30	179.96	173.99(3)

and S···O interactions are described in a very similar way by the two approaches on both geometric and topological grounds, the N4···H9 contact is longer in the gas-phase ge-

ometry than in the experimental one and the theoretical bond critical point (bcp) is therefore absent. In the optimised ab initio geometry an extra short intramolecular N−H⋯π contact is set up between the hydrogen atom of the acidic N6−HN6 group and the aromatic C17 atom. In agreement with one of the rules for the packing of hydrogen-bonded crystals proposed by Bertolasi et al.,[35] this bond does not occur in the crystal; instead the N6−HN6 group is involved in a competing intermolecular hydrogen bond with the N1 atom of the pyrimidinone ring of another molecule.[15]

The role of intramolecular non-covalent S⋯O interactions in the conformation and activity of biologically important systems has been investigated in the case of 1,4- and 1,5-type interactions.[36,37] The same role has been suggested in Paper 1 for the observed 1,6-type S⋯O close contact in **1** on the basis of the experimental geometry.[15] This hypothesis is now reinforced by the theoretical results, which indicate the same favourable interaction is also present in the gas-phase geometry. Interestingly, this fits very well with a feature observed in both AII and peptide AII antagonists such as Sarmesin in numerous quantitative structure–activity relationship (QSAR), conformational and modelling studies,[1c,4,38,39] which showed the existence of short, stabilising intramolecular contacts between the side-chain aromatic rings of the triad key amino acids Tyr⁴-His⁶-Phe⁸. As a result, the peptides assume a ring cluster conformation characterised by a charge relay system and recognised as essential for angiotensin II biological activity.

Atomic and molecular volumes: The exploration of the molecular volume and surface of a drug is frequently the first step to understanding drug action as the receptor cavity must usually be tightly filled with the interacting ligand to obtain an efficient and specific binding. In our theoretical calculations the in-crystal QTAIM[19] atomic volumes V_{cry} are defined by the interatomic boundaries in the crystal, whereas atomic volumes of isolated molecules, denoted by V_{001}, are based on a cut-off of $\rho = 0.001$ atomic units.

For a proper comparison with theory, we have also applied this cut-off to the experimental density, considering a single molecule extracted from the crystal (and nonetheless reflecting the interaction with the crystal environment) with the molecular boundaries artificially moved to infinity. The results are reported in full in the Supporting Information. In many cases, there are clear differences between V_{cry} and V_{001}, reaching more than 4 Å³ for sulfur and more than 2 Å³ for O3, N5 and C24. However, the charges are not affected, their values being practically equal within the experimental uncertainty. The molecular volume in the crystal is given by $\Sigma_\alpha V_{cry,\alpha} = 691.22$ Å³ and, when multiplied by $Z = 8$, reproduces the unit-cell experimental volume to within 0.2%. On the other hand, the sum of the V_{001} volumes (643.75 Å³) differs from the theoretical MCG-B3LYP molecular volume (662.64 Å³) of the isolated molecule by less than 3%. These results support the reliability and accuracy of the integration procedure.

Atomic and group charges: In the aspherical atom formalism of Stewart,[21] the experimental charge density $\rho_{exp}(\mathbf{r})$ is obtained as a superposition of atomic contributions $\rho_\alpha(\mathbf{r})$ [Eq. (1)], each one being modelled by the sum of two terms, a spherical part describing both the inner core of the atom and an unperturbed contribution to the valence and an aspherical one associated with the deformable valence and rendered by a multipolar expansion. Atomic contributions to $\rho_{exp}(\mathbf{r})$ are given formally by Equation (2), where the vector $\mathbf{p}_\alpha$ is in the form of a spherical tensor[7] and contains the monopole and higher multipole populations of atom α as obtained by least-squares refinement of the experimental structure-factor amplitudes, whereas the elements of vector $\mathbf{f}_\alpha(\mathbf{r})$ are nuclear-centred cartesian spherical harmonics[40] augmented with properly chosen radial functions.

$$\rho_{exp}(\mathbf{r}) = \sum_\alpha \rho_\alpha(\mathbf{r}) \tag{1}$$

$$\rho_\alpha(\mathbf{r}) = \mathbf{f}_\alpha(\mathbf{r})\mathbf{p}_\alpha \tag{2}$$

Unabridged cartesian moments of the charge density $\mathbf{m}_\alpha^{(l)}$ are obtained as expectation values [Eq. (3)] of the operator $x^i y^j z^k$ of rank $l = i + j + k$ ($i, j, k = 0, 1, 2, 3, ..$). In Equation (3) integration is extended over all the space pertaining to the nuclear centre α, whose electron density is given by Equation (2).

$$m_\alpha^{(l=i+j+k)} = \int x^i y^j z^k \rho_\alpha(\mathbf{r}) d\mathbf{r} \tag{3}$$

Equations (1), (2) and (3) introduce a *fuzzy* boundary partitioning of $\rho_{exp}(\mathbf{r})$ into atomic contributions that overlap each other, known as Stewart's pseudoatoms.[21b] On the other hand, Bader's quantum theory of atoms in molecules (QTAIM)[19] provides a unique *discrete* boundary partitioning of the real space of a molecule or crystal into submolecular regions, fragments or single atoms, to which all theorems of quantum mechanics apply. QTAIM moments are obtained by integrating the moment operator $x^i y^j z^k$ inside the atomic basin Ω_α of atom α [Equation (4)].[41]

Table 2. Experimental (first row) and theoretical (MOG-B3LYP, second row) geometrical and topological properties at the bond critical points (bcps) of the most relevant intramolecular interactions in LR-B/081.[a]

	H⋯A/X⋯A [Å]	⩽D-H-A [°]	ρ_{bcp} [e Å⁻³]	$\nabla^2\rho_{bcp}$ [e Å⁻⁵]
C9−H9⋯N4	2.751(6)	128.9(4)	0.043(3)	0.54(1)
	3.322	135.1	no bcp	
C5−H5A⋯O3	2.200(6)	126.3(4)	0.120(8)	1.74(7)
	2.192	129.0	0.121	1.51
S1⋯N5	3.2950(3)		0.050(1)	0.60(1)
	3.2212		0.061	0.68
S1⋯O1	3.1998(3)		0.063(2)	0.74(1)
	3.3064		0.047	0.58
N6−HN6⋯C17	3.161(9)	82.2(5)	no bcp	
	2.446	111.2	0.086	1.03

[a] Experimental standard uncertainties are given in parentheses.

$$m_\alpha^{(l=i+j+k)} = \int_{\Omega_\alpha} x^i y^j z^k \rho(\boldsymbol{r}) \mathrm{d}\boldsymbol{r} \qquad (4)$$

The zeroth-rank moments $m_\alpha^{(0)} = p_\alpha^{(0)}$ give the atomic population, that is, the total number of electrons, of atom α. Hereinafter they will be replaced by the atomic net charge $q_\alpha = Z_\alpha - m_\alpha^{(0)}$, where Z_α defines the nuclear charge of atom α.

Stewart's charges, as obtained through the multipolar refinement of the X-ray data, have been reported in Paper 1:[15] in addition, both the experimental and the theoretical (MCG-B3LYP and MOG-B3LYP) $\rho(\boldsymbol{r})$ of LR-B/081 have now been analysed in terms of the QTAIM[19] DMA and the results are reported in full in the Supporting Information. The experimental and theoretical MCG-B3LYP values are fairly well correlated ($q_{\text{expt}} = 0.92(2)q_{\text{theo}}$, $r = 0.988$, Figure 2), although the theoretical values are slightly overestimated compared with the experimental values, as found recently by Abramov and co-workers.[42] In Figure 3b the distribution of the experimental QTAIM charges is graphically
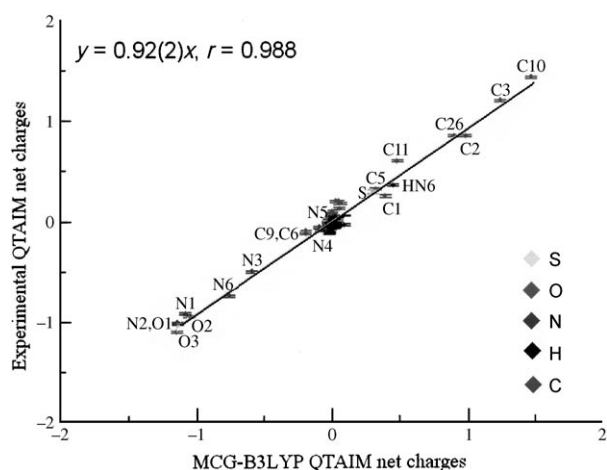

Figure 2. Linear correlation between experimental and MCG-B3LYP values of QTAIM charges (e). The standard uncertainties of the experimental charges are reported as vertical bars.
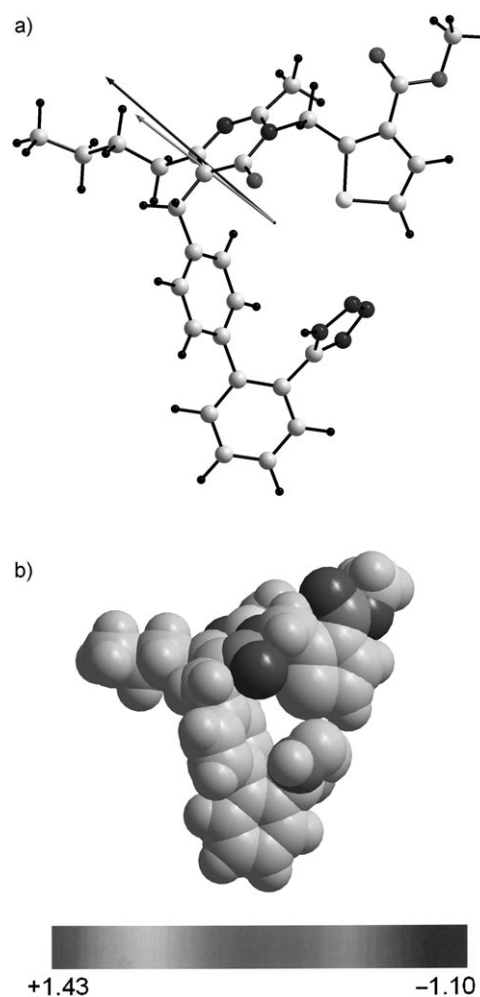

Figure 3. a) Experimentally determined molecular structure of LR-B/081 at 17 K. The dark and light arrows indicate the direction of the experimental dipole vector obtained from Stewart and Bader partitioning of the electron density, respectively. b) van der Waals surface of LR-B/081 in the crystal form. The colour code indicates the experimental QTAIM net atomic charges and ranges from +1.43 (red) to −1.10 electrons (blue).

displayed on the van der Waals surface of **1**: this visual rendering allows a sort of "painting" of the surface of the molecule according to atomic charges, indicating the presence of polar/apolar groups. Figure 3b shows that most of the atoms (ca. 80%) have atomic charges close to zero, but when summing the atomic charges of specific fragments or functional groups of the molecule, the group charges (Table 3) reveal the presence of regions where the electron distribution is concentrated (as in the central pyrimidinone ring, the terminal tetrazole ring and the methyl ester moiety) and depleted (as in the bridging methylene group between the thiophene and pyrimidinone rings and in the butyl chain). As a whole, the charge distribution in **1** is not characterised by a unique electrophilic region opposed to a nucleophilic area, but rather by a mixture of electropositive and electronegative zones. Indeed, charges of opposite sign, rather than being

Table 3. Group charges from QTAIM partitioning of the electron density.[a]

Group	Experimental	MCG-B3LYP	MOG-B3LYP
pyrimidinone	−0.72(4)	−0.747	−0.736
C(12)H$_3$	0.162(8)	0.143	0.141
n-butyl	0.206(9)	0.098	0.096
tetrazole	−0.177(6)	−0.155	−0.167
thiophene	0.10(1)	0.093	0.087
methyl ester	−0.12(3)	−0.151	−0.151
p-phenyl	−0.019(7)	0.003	−0.008
o-phenyl	0.041(9)	0.108	0.136
C(13)H$_2$[b]	0.103(8)	0.094	0.094
C(5)H$_2$[c]	0.436(7)	0.514	0.509

[a] All values are in electrons. Experimental standard uncertainties are given in parentheses. [b] Bridging methylene between biphenyl and pyrimidinone moieties. [c] Bridging methylene between thiophene and pyrimidinone moieties.

well separated, are markably mixed, as indicated also by the short distance between the centres of positive and negative charges (0.2 Å for experimental QTAIM values).

The differences between the experimental (in-crystal) and theoretical (isolated molecule) charges hint at the degree of polarisation of the electron distribution due to the intermolecular interactions: in the crystal the butyl chain becomes significantly more positive and the o-phenyl group less positive, meaning that some electronic charge is transferred from one end of the molecule to another upon crystallisation.

We also note that both the experimental and the theoretical QTAIM charges confirm the electrostatic nature of the S···N and S···O interactions discussed in Paper 1.

Molecular electrostatic moments: These quantities provide a concise summary of the nature of the charge distribution over the molecule: the monopole (the electric moment of rank zero) represents the total charge and the higher poles are a measure of the charge separation.

The molecular electrostatic moments of **1** have been calculated up to the fourth rank by shifting all atomic moments m_α to a common origin,[43] the centre of mass of the molecule, and then summing the results [Eq. (5)]. The shift matrices $S_\alpha(R_\alpha - R_o)$[33,43] depend on the cartesian coordinates of the nuclear centre α, R_α and of the molecular centre of mass R_o.

$$m_{mol} = \sum_\alpha S_\alpha(R_\alpha - R_o) m_\alpha \tag{5}$$

The molecular moments obtained through Equation (5) are invariant with respect to the partitioning scheme used to evaluate the atomic moments m_α;[44] for periodic systems, this holds only if the asymmetric unit contains no more than one molecule, as in the case of **1**, and fuzzy partitioning schemes are used. As fuzzy molecules have boundaries at infinity, fuzzy partitionings of periodic electron densities (like Stewart[21] and Mulliken[45] DMAs) yield molecular moments that refer to a molecule removed from the crystal. QTAIM discrete partitioning of periodic electron densities may give two different results depending on the definition of molecular boundaries. When molecular boundaries are moved artificially to infinity (by the same criterion as used in the previous section to evaluate V_{001} so that the molecule is removed from the crystal), QTAIM molecular moments are identical to Stewart molecular moments within numerical accuracy. On the other hand, when molecular boundaries are defined by the interatomic boundaries in the crystal, then the real in-crystal molecular moments are obtained.

The molecular first and second moments of **1**, based on a number of partitioning schemes applied to the present experimental and theoretical electron densities, are listed in Table 4 and Table 5, respectively, and higher order moments are graphically visualised in Figure 4 and Figure 5. Further details are reported in the Supporting Information. All components are referrred to the inertial reference system of co-

Table 4. Experimental and theoretical molecular dipole moments [debye] of **1**.[a]

	Experimental Stewart[b]	QTAIM[c]	MCG-B3LYP	Theoretical MOG-B3LYP[d]	P-B3LYP[e]
$|\mu|$	6.8(15)	5.4(14)	2.88	3.64	1.48
μ_x	2.2(21)	1.5(20)	−2.47	−0.52	−0.44
μ_y	−6.4(16)	−5.0(14)	−1.38	−3.59	−1.30
μ_z	−0.8(6)	−1.3(5)	−0.56	−0.26	−0.54

[a] The component values refer to the inertial coordinate system with the origin at the centre of mass. Experimental standard uncertainties are given in parentheses. [b] Calculated from Stewart's atomic populations. [c] Calculated from Bader's atomic basins. [d] The components are in the rotated coordinate system which maximises the overlap between the experimental and the optimised geometries. [e] Calculated from Mulliken DMA.

Table 5. Experimental and theoretical components of the molecular second moment $m^{(2)}$ [buckingham = debye Å] of **1**.[a]

	Experimental Stewart[b]	QTAIM[c]	MCG-B3LYP	Theoretical MOG-B3LYP[d]	P-B3LYP[e]
m_{xx}	−202(12)	−193(10)	−193	−197	−194
m_{yy}	−214(11)	−215(10)	−236	−249	−228
m_{zz}	−244(7)	−237(5)	−247	−246	−235
m_{xy}	8(9)	9(6)	5	13	7
m_{xz}	14(5)	16(3)	17	10	14
m_{yz}	1(5)	2(2)	−1	−5	1
isotropic value[f]	−220(6)	−215(5)	−225	−230	−219
anisotropy[g]	6.9(9)	7.0(7)	7.6	7.7	6.9
asphericity[h]	0.030	0.076	0.043	0.052	0.030

[a] The component values refer to the inertial coordinate system with the origin at the centre of mass. Experimental standard uncertainties are given in parentheses. [b] Calculated from Stewart's atomic populations. [c] Calculated from Bader's atomic basins. [d] The components are in the rotated coordinate system which maximises the overlap between the experimental and the optimised geometries. [e] Calculated from Mulliken DMA. [f] One third of the trace of $m^{(2)}$. [g] See text for definition. [h] Obtained from Equation (6).
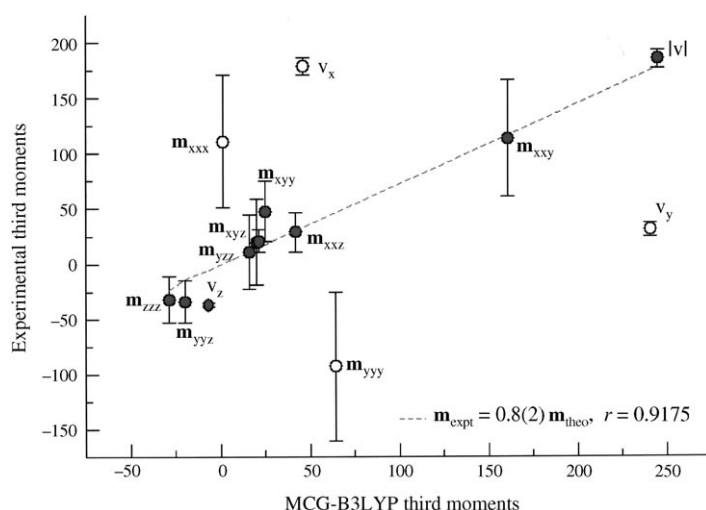

Figure 4. Linear correlation between experimental and MCG-B3LYP values (in debye Å²) of the third moments of **1**. The standard uncertainties of the experimental values are reported as vertical bars.
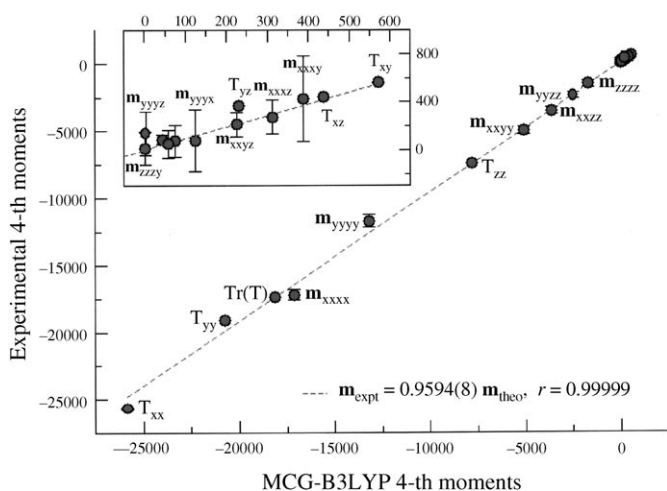
Figure 5. Linear correlation between experimental and MCG-B3LYP values (in debye Å³) of the fourth moments of **1**. The standard uncertainties of the experimental values are reported as vertical bars. The inset is an enlargement of the upper right corner of the main graph.

ordinates with the origin at the centre of mass of the molecule.

Dipole moments: The magnitude of the dipole vector, whose components provide a measure of the polarity of a molecular charge distribution, was found to be $|\mu| = 6.8(15)$ debye (D) from the Stewart partitioning of the experimental $\rho(r)$ applied to the molecule extracted from the crystal. The value decreases to 5.4(14) D when the QTAIM partitioning is applied to the molecule in the crystal form (Table 4). The two vectors point in the same direction, that is, towards the butyl chain, the angle between them amounting to about 8° (Figure 3a). This confirms the findings on the atomic charges and agrees with the results of previous studies on **1**,[3,15] which showed a large region of positive long-range potential around the 6-butyl chain which is believed[1a] to fit into a lipophilic pocket of the receptor that accommodates the Ile⁵ side-chain of AII. In the crystal the dipole moment is oriented almost parallel to the crystallographic [010] direction, with an angle between μ_{exp} and the *b* axis of 2° for Stewart's vector and of 10° for the QTAIM one. Regardless of the choice of partitioning scheme, the standard uncertainties (s.u.) are quite large: 24–28% for the most significant *y* component, 38–75% for the *z* component and 95–130% for the *x* component, meaning that within 2 s.u.s the dipole moment is either halved or increased by about 50%.

For the isolated molecule in the crystal geometry the magnitude of the dipole vector is $|\mu| = 2.88$ D (MCG-B3LYP). Full geometry relaxation of the molecule in the gas phase enhances the dipole moment by 26% up to 3.64 D (MOG-B3LYP). The largest difference between the dipole moment directions derived from experiment and theory is approximately 79° for the isolated molecule in the crystal geometry and decreases to about 36° after molecule optimisation. By considering the QTAIM value as the best experimental esti-

mate of the dipole moment and the MCG-B3LYP value as the reference, the dipole moment enhancement, occurring upon crystallisation as a consequence of both crystal field effects and intermolecular interactions, is about 87%, whereas, with respect to the MOG-B3LYP value, the enhancement is reduced to 48%, again high, but quite close to the range of 30–40% reported in the literature as typical for hydrogen-bonded systems.[46,47] In an attempt to calculate the ab initio value of μ in the crystal, we performed fully periodic DFT calculations on the 17 K experimental geometry with the CRYSTAL2003 program.[30] However, as this version of the code (the only one that can handle a structure as large as **1**) does not include QTAIM analysis of the electron density, we could only derive a value for the dipole moment from the periodic Mulliken DMA, as retrieved from the wavefunction of the CRYSTAL2003 program by the code PAMoC.[33] We have obtained a value of 1.48 D (P-B3LYP, Table 4), which differs by less than 3 s.u.s from the experimental QTAIM estimate, but is certainly much lower than expected, as it contradicts the enhancement of the molecular dipole moment commonly observed on crystal formation.[48] The angle between the experimental and the P-B3LYP dipole moments is between 35 and 40°, depending on the scheme adopted to partition the experimental $\rho(r)$, and is mainly determined by the *x* components, which have opposite signs.

The P-B3LYP result was confirmed by an MCG-B3LYP calculation on a molecule of **1** embedded in a field of 41 930 point charges obtained by a QTAIM analysis of the theoretical (MCG-B3LYP) electron density and located at the atomic positions in the crystal: the interaction with the background of point charges yielded a dipole moment of 1.76 D. On the other hand, a multipole refinement of the theoretical P-B3LYP structure factors, performed with the VALRAY code with the same multipole model described in Paper 1 for the refinement of experimental structure factors, yielded a large molecular dipole moment of 11.1(6) D, and an early evaluation of $|\mu|$ from a multipole refinement of our experimental data with the XD code[49] gave an even larger value of 13.8(28) D. A detailed investigation of this issue is beyond the scope of this paper and will be reported separately.[50]

Second moments: These moments provide a second-order approximation of the total electron distribution, giving at least a crude idea of its shape: their reliability as derived from low-temperature high-quality X-ray diffraction data sets has been widely proved by the work of Spackman and co-workers.[14,51,52] Nevertheless, very few studies on molecular quadrupole moments extracted from experimental charge-density analyses have been reported so far.[52,53]

In the case of a non-symmetric molecule, such as **1**, the six components of the second moment tensor are all independent and their relationship to charge contraction/expansion along a particular direction defined by some structural elements (e.g., a bond axis) is not as straightforward as in simpler cases.[46,52,54]

The isotropic value of the molecular second moment in **1**, calculated as one third of the trace of the second moment tensor $\boldsymbol{m}^{(2)}$, is −219.0 buckingham (B) in the crystal form (P-B3LYP) and is slightly more negative in the isolated molecule in the crystal (−225.4 B, MCG-B3LYP) and optimised (−230.6 B, MOG-B3LYP) geometries. From an inspection of Table 5, it can be seen that 1) the experimental values of the tensor components are in excellent, quantitative agreement with the theoretical ones and 2) the experimental s.u. of the diagonal elements of the tensor are very small (<6% of the corresponding quantity). This implies that, at variance with the molecular first moment, the second moment of **1** is highly significant and well-determined. The Λ_x, Λ_y, and Λ_z principal values (not reported here) differ by less than 14–18% from the isotropic value, indicating a nearly spherical electron density distribution. This may be quantified by introducing the asphericity parameter A[55] given by Equation (6).

$$A = [\tfrac{1}{2} \sum_{i>j} (\Lambda_i - \Lambda_j)^2 / (\sum_i \Lambda_i)^2]^{\tfrac{1}{2}} \tag{6}$$

As shown in Table 5, the values calculated for A for the crystal and the isolated molecule are close to zero, as expected for spherically symmetric objects.[56] Another measure of anisotropy, reported in Table 5, is given by the trace relationship $(\tfrac{1}{2}[3\mathrm{Tr}(\boldsymbol{m}^2) - (\mathrm{Tr}\boldsymbol{m})^2])^{\tfrac{1}{2}}$, which defines the deviation from the isotropic value, and is about 3% for **1**. The only significant *trans*-axial distortion of the ellipsoid is given by the xz off-axis component of 14 debye Å.

The almost equal distribution of molecular charge in the three directions of space explains why the first moments are scarcely significant and ill-determined, whereas the second moments are large, significant and highly reliable. Similar considerations apply to the third and fourth moments, as described in the next section.

Higher order moments: To the best of our knowledge, X-ray-derived third moments have been reported in the literature in only three cases[57–59] and molecular fourth moments have been published only once as Supporting Information.[60] This is probably because their direct interpretation in terms of charge density distribution is not as straightforward as for the lower moments.

The experimental third and fourth moments of **1** derived from QTAIM partitioning of the electron density are compared with the corresponding MCG-B3LYP values in Figure 4 and Figure 5.[61] The components $v_i = \Sigma_j m_{ijj}$ ($i,j = x,y,z$) and the magnitude $|\boldsymbol{v}|$ of the vector part of the third moment tensor are also reported in Figure 4, whereas Figure 5 shows, in addition to the m_{ijkk} components, the elements $t_{ij} = \Sigma_k m_{ijkk}$ ($i,j,k = x,y,z$) of the matrix part of the fourth moment tensor together with its isotropic value $t_{iso} = \tfrac{1}{2}\mathrm{Tr}\boldsymbol{t}$. As for the first moments, least-squares uncertainties in the third moments are quite large so that their estimated values are not statistically very significant. When compared with the theoretical results, the m_{xxx} and m_{yyy} elements differ both in magnitude and sign and these discrepancies are reflected in the v_x and v_y vector components. Still, it is worth noting that the remaining components have values that are in fair agreement with calculated values.

The fourth moments are large and rather well determined, further pointing to a nearly spherical charge distribution. The agreement between experimental and theoretical results is almost quantitative (Figure 5) in spite of the fact that the components that are expected to be small or null for a spherical charge distribution (i.e., s^3t and s^2tu, where $s,t,u = x,y,z$) are affected by large least-squares errors.

At the request of one of the referees, we mention here that the experimental electric moments of **1** obtained from a less extended multipolar model ($L_{max} = 4$ for the sulfur atom and $L_{max} = 3$ for the nitrogen, oxygen and carbon atoms) are equivalent within 1.5 s.u. to those discussed above. The presence of hexadecapoles on all non-hydrogen atoms is therefore confirmed as essential to properly locate the bcp of the S1···O1 interaction (as discussed in Paper 1), but has a limited impact on the values of the electric moments. Full details of the experimental electric moments as obtained with the less extended multipolar model are reported in the Supporting Information.

Hydrogen bond energetics: The crystal structure of **1** shows one NH···N intermolecular hydrogen bond connecting the acidic tetrazole ring of one molecule with the pyrimidinone system of another and 11 intermolecular short contacts of the CH···X type (with X = O, S or N): in Paper 1 all these interactions were classified as true hydrogen bonds on the basis of topological criteria.[15,62] The four hydrogen-bonded molecular pairs (hereinafter dimers or dimeric adducts) resulting from these interactions are denoted with letters A–D in Table 6. Dimer A, whose two molecules are related to each other by the crystallographic glide plane *c*, has five different hydrogen bonds that are responsible for the formation of infinite ribbons running along the *c* axis. Contiguous ribbons along the *a* axis are related by two-fold screw axes and linked by the C22−H22···N3 interaction, forming dimer D (Figure 6a). The five hydrogen bonds of dimer B, whose two molecules are 9.443 Å apart and are related by a 2_1 axis, account for zigzag ribbons extending along the *b* axis (Figure 6b), whereas the C11−H11C···N3 hydrogen bond of pair C, occurring twice because of a centre of inversion, relates the two molecules in a head-to-tail fashion.

To gain a deeper insight into the fundamental nature of intermolecular hydrogen bonds and to rank their strength on a relative scale, it is crucial to obtain reasonable estimates of their energies: to this end, it must be noted[63] that the theoretical and experimental values of the total intermolecular interaction energy (E_{int}) should not be quantitatively associated with the hydrogen bond energy as the intermolecular hydrogen bonds are not the only and not necessarily the main contributions to E_{int}.

We followed the approach proposed by Abramov[64] for closed-shell interactions including hydrogen bonds in which the kinetic energy density $G(\boldsymbol{r})$ at the bond critical points is

Table 6. Estimates of the kinetic energy density ($G(\boldsymbol{r})_{bcp}$), local potential energy density ($V(\boldsymbol{r})_{bcp}$) and bond energies ($-E_{HB}$) from the experimental topological indicators of the intermolecular hydrogen bonds.

Pair[a]	Bond	$d_{H\cdots A}$ [Å]	$G(\boldsymbol{r})$ [kJ mol⁻¹ bohr⁻³][b]	$V(\boldsymbol{r})$ [kJ mol⁻¹ bohr⁻³][c]	$-E_{HB}$ [kJ mol⁻¹][d]
A	N6−HN6···N1	1.871(10)	62(2)	−98(4)	49
A	C12−H12A···N5	2.329(6)	24.4(6)	−20.1(9)	10.0
A	C12−H12C···O1	2.345(7)	20.2(5)	−15.3(7)	7.6
A	C5−H5B···O2	2.460(6)	18.3(4)	−14.6(6)	7.3
A	C12−H12A···S1	3.068(6)	10.7(3)	−7.8(3)	3.9
B	C12−H12B···N5	2.553(6)	15.4(4)	−11.5(5)	5.7
B	C5−H5A···N4	2.677(6)	15.0(3)	−11.3(4)	5.6
B	C28−H28B···O2	2.743(6)	9.7(3)	−6.4(3)	3.2
B	C9−H9···N2	2.941(6)	8.6(2)	−5.7(2)	2.9
B	C30−H30B···O3	2.994(6)	5.9(2)	−3.7(2)	1.9
C	C11−H11C···N3	2.508(7)	16.3(4)	−13.3(6)	6.6
D	C22-H22···N3	2.516(6)	17.6(4)	−13.8(6)	6.9

[a] Symmetry operations relating the second molecule of a pair to the parent one (at x,y,z) are for A: $x,\frac{1}{2}-y,-\frac{1}{2}+z$; B: $-x,\frac{1}{2}+y,\frac{1}{2}-z$; C: $-x,-y,1-z$; D: $\frac{1}{2}-x,-y,-\frac{1}{2}+z$. [b] The kinetic energy density was evaluated according to Equation (7), see ref. [64]. [c] The local potential energy density was evaluated by the application of the local statement of the virial theorem {Eq. (8), see ref. [65]}. [d] Estimated using Equation (9): $E_{HB}=0.5V(\boldsymbol{r})_{bcp}$.

related to the experimental topological parameters through Equation (7) and to the potential energy density $V(\boldsymbol{r})$ through the local statement of the virial theorem[19] expressed by Equation (8).
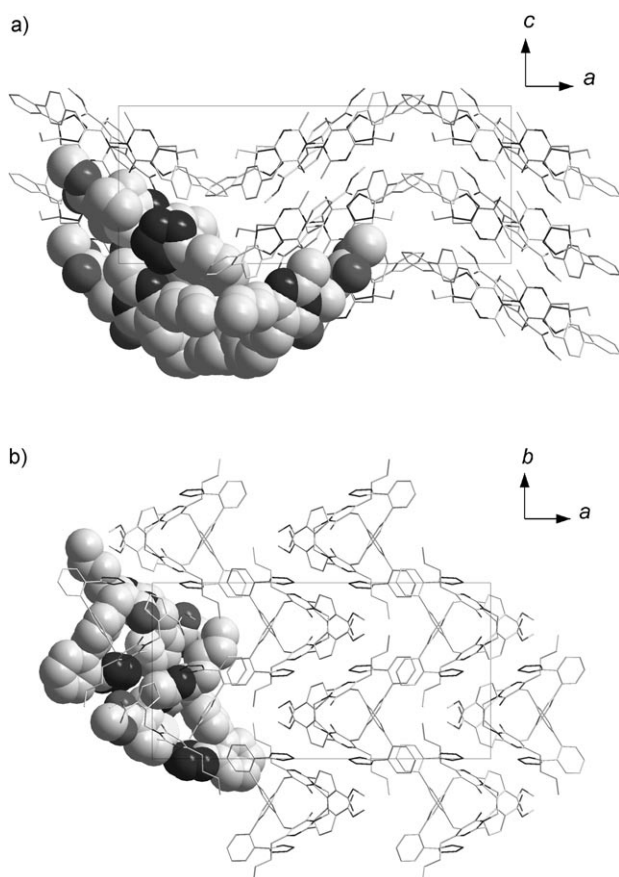

Figure 6. Three-dimensional supramolecular architecture of **1** viewed along a) the b axis and b) the c axis. Hydrogen atoms have been omitted for clarity.

$$G(\boldsymbol{r})_{bcp} = \tfrac{3}{10}(3\pi^2)^{\frac{2}{3}}[\rho(\boldsymbol{r})_{bcp}]^{\frac{5}{3}} + \tfrac{1}{6}\nabla^2\rho(\boldsymbol{r})_{bcp} \quad (7)$$

$$V(\boldsymbol{r})_{bcp} = \tfrac{1}{4}\nabla^2\rho(\boldsymbol{r})_{bcp} - 2G(\boldsymbol{r})_{bcp} \quad (8)$$

The results obtained by applying these relationships to the experimental $\rho(\boldsymbol{r})$ of **1** for each of the 12 intermolecular hydrogen bonds are listed in Table 6, where the reported values of $V(\boldsymbol{r})_{bcp}$ are to be considered as estimates, as the multipole-derived charge density does not obey the local virial theorem. The relationship between the two local electronic energy densities, $G(\boldsymbol{r})_{bcp}$ and $V(\boldsymbol{r})_{bcp}$, is shown in Figure 7. A fair linear dependence is obtained for all the weak CH···X hydrogen bonds, in agreement with results reported by Espinosa et al.[65] for a series of molecular dimers involving XH···O hydrogen bonds (X=C, N and O), but a quadratic fitting is even more applicable (correlation coefficient of −0.9997) to the whole range of YH···X interactions despite the different chemical nature of the species involved.
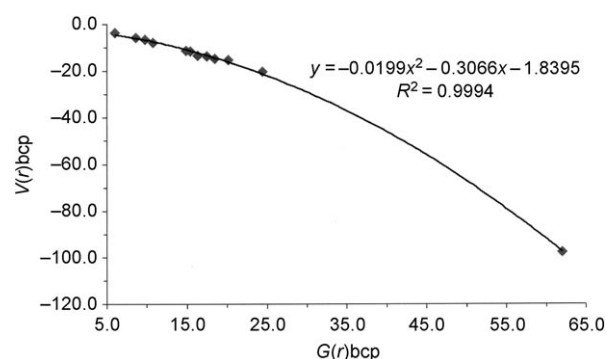

Figure 7. $V(\boldsymbol{r})_{bcp}$ versus $G(\boldsymbol{r})_{bcp}$ for the intermolecular hydrogen bonds of **1**. Values are in units of kJ mol⁻¹ bohr⁻³. The quadratic equation resulting from the least-squares fit for all the hydrogen bonds is also reported.

The same authors showed that for closed-shell interactions the hydrogen bond energy E_{HB} (defined as $-D_e$, where D_e is the hydrogen bond dissociation energy) may be correlated to the $V(\boldsymbol{r})_{bcp}$ value through the relationship given by Equation (9).

$$E_{HB} = 0.5V(\boldsymbol{r})_{bcp} \quad (9)$$

We are aware of the criticism that has been raised towards such a relationship,[66] but have preferred to maintain the

original empirical relationship of Espinosa et al. (as done recently by Zhurova et al.[67]) mainly because our purpose was simply to place the strengths of the hydrogen bonds on a relative scale and other alternative equations appeared suitable only for a specific kind of hydrogen bond without covering the full range of interactions shown by **1**.[68]

Our results are reported in the last column of Table 6. As expected, the NH⋯N hydrogen bond is predicted to be the most attractive bond with an energy of almost 50 kJ mol^{-1}: note that the value of the potential energy density $V(r)$ for this hydrogen bond ($-98(4)$ kJ mol^{-1} bohr^{-3}) is very close to the value of -91.89 kJ mol^{-1} bohr^{-3} reported[69] for a similar intermolecular interaction in crystals of histidine, which is the sixth residue in the octapeptide AII. The NH⋯N hydrogen bond found in those crystals is very similar to that observed in **1** with an H⋯N bond distance of 1.82 Å (1.871 Å in **1**) connecting one N(sp^3)−H hydrogen atom to the N(sp^2) nitrogen atom of the imidazole ring through the same symmetry relation that exists in dimer A of our compound. The relevance of such a similarity to the understanding of the peptidomimetic action of milfasartan at the AT$_1$ receptor will be discussed in depth in a forthcoming paper.[70]

Hydrogen bonds as pharmacophoric features: The values of the CH⋯O interaction energies reported in the literature[71] range between around 1 kJ mol^{-1} in the case of very weak hydrogen bonds and 9.5 kJ mol^{-1} for polarised bonds: from an inspection of Table 6 it can be seen that the three oxygen atoms of **1** are all involved as acceptors in CH⋯O hydrogen bonds and that their corresponding $-E_{HB}$ values lie in the medium range 1.9–7.6 kJ mol^{-1}. The CH⋯N interactions have been studied less, but their "subtle but important roles in biological systems, at least when hydrophobic pockets are involved" have been pointed out quite recently by means of electrochemical and density functional analyses of pyrimidine pairings.[72] All five N(sp^2) nitrogen atoms of **1** (three in the tetrazole ring and two in the pyrimidinone fragment) are engaged as acceptors in NH⋯N and CH⋯N hydrogen bonds, the latter with energies between 2.9 and 10 kJ mol^{-1}.

The C12 methyl group forms four different hydrogen bonds with nitrogen, oxygen and sulfur atoms as acceptors. Among these interactions, the C12−H12A⋯N5 hydrogen bond stands out as the most attractive, having an energy of 10 kJ mol^{-1}. This means that this substituent group of the central pyrimidinone ring can offer an efficient proton donor site for interactions of the CH⋯X type with the receptor, providing a significant energetic contribution to the total binding energy. This pharmacophoric feature closely resembles that reported for the acidic CH group between the two nitrogen atoms of imidazole in a recent survey of histidine residues in proteins,[73] further proving that the His^6 residue in AII can be mimicked by the pyrimidinone ring in sartan drugs and that they probably share the same binding mode to the AT$_1$ receptor. Conversely, out of the 10 CH aromatic groups, only two, the C9−H9 bond of the thiophene and the C22−H22 of the *o*-phenyl ring, are weakly acidic and give rise to hydrogen bonds, hinting that the interaction

with the receptor at these sites is dominated by dispersion forces.

Finally, note that the two hydrogen atoms of the C5 methylene group are both involved in hydrogen bonds (with energies of 7.3 and 5.6 kJ mol^{-1}, respectively): this strongly suggests that the role of this fragment is not just that of a spacer between the thiophene and the pyrimidinone moieties, but rather that it participates actively in the drug–receptor interaction.

Energies of intermolecular interactions: Non-covalent interaction energies are computed as the difference in energy between the dimer and the sum of the isolated monomers [Equation (10)].

$$E_{int} = E(AB) - [E(A) + E(B)] \tag{10}$$

There are a variety of ways in which E_{int} can be partitioned, but the scheme that has received the most use over the years in theoretical calculations is the Morokuma–Ziegler decomposition scheme[74,75] expressed by Equation (11), where E_{es} is the electrostatic interaction energy defined by the exact potential (EP), E_{Pauli} is the exchange repulsion and E_{oi}, the orbital interaction energy, includes charge transfer and polarisation effects. Conversely, when the starting point is an X-ray charge density distribution, a convenient formalism is given by Equation (12).[76,77] Here E_{es} is calculated according to the Buckingham-type (moment–moment, MM) approach,[6] the repulsion (E_{rep}) and dispersion (E_{disp}) terms are approximated using *exp-6* atom–atom potentials and E_{pen} is defined as the interaction of the spherical charge distribution of one molecule with the deformation charge density of the second. Hydrogen bonds are described by omitting the atom–atom repulsive potential terms between the proton and its acceptor.[77]

$$E_{int} = E_{es} + E_{Pauli} + E_{oi} \tag{11}$$

$$E_{int} = E_{es} + E_{rep} + E_{disp} + E_{pen} \tag{12}$$

Electrostatic interaction energies: The theoretical and experimental estimates of the electrostatic contribution to the total interaction energy for the four hydrogen-bonded dimers of **1** and for two other pairings with short intermolecular contacts (Figure 8) are summarised in Table 7. The third column reports experimental values of E_{es} as obtained from the multipolar X-ray-derived $\rho(r)$ through the MM approximation corrected for the promolecule energy following the strategy recently proposed by Spackman[78] and implemented in the PAMoC code.[33] In this approach, E_{es} is expressed as the sum of promolecule–promolecule, promolecule–deformation and deformation–deformation terms [Eq. (13)], where $E_{pro-pro}$ is the sum of the coulombic interactions between pairs of spherical atomic charge densities and can be determined as a function of their separation, $E_{def-def}$ is the "old" MM electrostatic component of Equation (12) arising from the deformation terms of the molecular charge
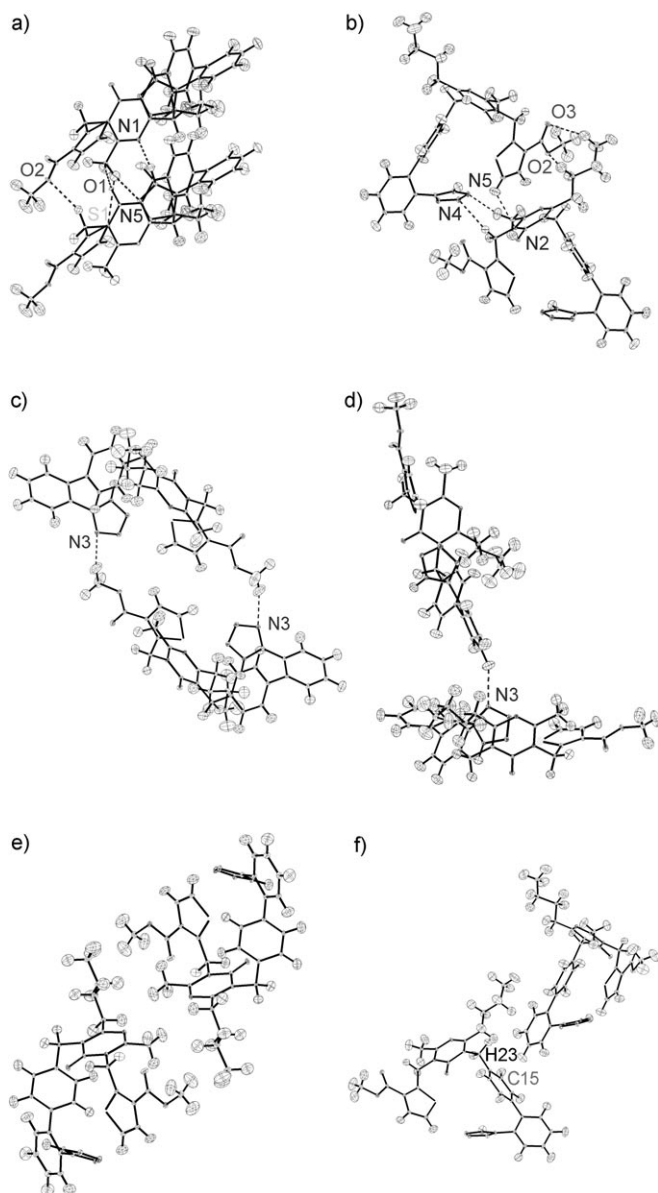
Figure 8. ORTEP plot of six molecular pairs of **1**. Ellipsoids at the 50% probability level. Intermolecular hydrogen bonds, where present, are represented as dashed lines.

Table 7. Comparison between values of the electrostatic contribution to the total interaction energies for six molecular pairs of **1**, as evaluated by different methods.

Pair[a]	d_{CM} [Å][b]	E_{es} [kJ mol^{-1}]	
		Experimental[c]	MCG-BLYP[d]
A	6.037	−98(3)	−125
B	9.443	−26(2)	−31
C	11.356	−23(4)	−19
D	13.365	−5(2)	−11
E	12.312	−3(2)	−3
F	12.389	−22(2)	−17

[a] Symmetry operations relating the second molecule of a pair to the parent one (at x,y,z) are for A: $x,\frac{1}{2}-y,-\frac{1}{2}+z$; B: $-x,\frac{1}{2}+y,\frac{1}{2}-z$; C: $-x,-y,1-z$; D: $\frac{1}{2}-x,-y,-\frac{1}{2}+z$; E: $-x,1-y,1-z$; F: $\frac{1}{2}-x,\frac{1}{2}+y,z$. [b] Distance between the centres of mass of the molecules in a pair. [c] Electrostatic energy obtained through Equation (13) (see text) applied to the experimental $\rho(\mathbf{r})$. The s.u. of the $E_{def\text{-}def}$ term is given in parentheses. [d] Electrostatic contribution to the interaction energy obtained from MCG-BLYP calculations on the isolated dimers (ADF program).

$$E_{es} = E_{pro\text{-}pro} + E_{def\text{-}def} + E_{pro\text{-}def} \qquad (13)$$

We note that for all the dimers the contribution of the $E_{pro\text{-}pro}$ term to the electrostatic energy is large and, with the exception of dimer D, it is more negative than the quantity $E_{def\text{-}def}$. In particular, for dimers A, B and F, $E_{pro\text{-}pro}$ contributes from 74 to 88% to the total (attractive) electrostatic energy, whereas for dimer C the two contributions are comparable (−11 and −13 kJ mol^{-1} for $E_{def\text{-}def}$ and $E_{pro\text{-}pro}$, respectively) and in dimer E, for which the $E_{def\text{-}def}$ term is repulsive (+6 kJ mol^{-1}), the $E_{pro\text{-}pro}$ contribution (−10 kJ mol^{-1}) makes the total electrostatic energy attractive. From an inspection of Table 7, the following points can be noted.

1) For all six dimers, the E_{es} values are always negative.
2) The agreement between the experimental estimates of E_{es} and those from the exact potential is more than satisfactory, the new Spackman model for E_{es} predicting the correct relative electrostatic interaction energies with no exceptions.
3) As expected, the highest value in modulus is found for dimer A, whose strong NH···N hydrogen bond accounts for the energetically most favourable dimer configuration. By considering, to a first approximation, the hydrogen bond energies reported in the preceding section to be on the same scale as the E_{es} values, we observe that the hydrogen bond energies of this pair account for almost 80% of the electrostatic term. The remaining 20% is due to attractive electrostatic interactions other than hydrogen bonds, including C12···HN6 (at 2.905 Å and −12 kJ mol^{-1}) and C9···H13B (at 2.912 Å and −8 kJ mol^{-1}).
4) Dimer B and C have comparable values of E_{es} although the percentage of the E_{HB} contribution is significantly different (74 and 58% for dimer B and C, respectively). The remaining stabilisation in pair C is due to other significant attractive interactions, such as C9···H8 (at

distribution and $E_{pro\text{-}def}$ is the E_{pen} component of Equation (12). The $E_{def\text{-}def}$ part was evaluated from the atom-centred multipole expansion up to the hexadecapole–hexadecapole term in the cartesian tensor formulation. The convergence of the multipole series was tested by examination of the contributions of terms with increasing power of $1/R$, that is, the reciprocal of the internuclear distance: for the quadrupole–hexadecapole terms we found a maximum contribution of 0.59 kJ mol^{-1}, for the octupole–octupole terms 0.11 kJ mol^{-1} and for the hexadecapole–hexadecapole contributions 0.01 kJ mol^{-1}. The fourth column reports the electrostatic interaction energies as obtained with the ADF program[25,26] for the isolated dimers.

3.188 Å and -6 kJ mol^{-1}) and N4$\cdots$H11C (at 2.634 Å and -4 kJ mol^{-1}).

5) Dimer F, although devoid of hydrogen bonds, has an E_{es} value that is comparable to those of dimers B and C. This is mainly due to the large contribution of the $E_{pro-pro}$ term (-17 kJ mol^{-1}, that is, 77% of the total E_{es}) and to the presence of some favourable atomic interactions. In this pair, because of the orientation of the two molecules, which are related by the glide plane b, the o-phenyl ring of one molecule directly faces the butyl chain and the p-phenyl group of the other whereas the remaining parts of the two molecules, being far from each other, do not form significant short contacts (Figure 8). The extra attractive MM contribution can then be attributed to the favourable interaction between the facing moieties. The dimer conformation is such that the average plane through the carbon atoms of the butyl chain of one molecule forms an angle of 11° with the average plane of the o-phenyl group of the other (minimum distance of 2.771 Å between the H21 and H7C atoms), whereas the o- and p-phenyl rings are oriented in an edge-to-face (T-shaped) arrangement (the angle between the ring planes amounting to 81° with a minimum distance of 2.528 Å between the H23 and C15 atoms). This is known to be the most favourable orientation for aromatic–aromatic interactions, having in addition to the dispersion term a significant electrostatic component (in the range of between 4 and 12 kJ mol^{-1}).[18] Dimer F closely fits this situation and our data provide a quantitative estimate of the energy involved.

Total interaction energies: Table 8 shows E_{int} values evaluated as follows: through Equation (12) applied to the experimental (third column) $\rho(\boldsymbol{r})$ of the crystal form, through Equation (11) applied to ADF MCG-BLYP calculations (fourth column) and through Equation (10) applied to supermolecule MCG-B3LYP calculations (fifth column). The values in the last two columns take into account the correction for the BSSE through the counterpoise method.[32] The following points can be noted.

1) Pair A, although having the largest attractive electrostatic energy, is not the most favoured, having a total experimental energy of just -10 kJ mol^{-1}. Because of the orientation of the two molecules, whose centres of mass are separated by only 6.037 Å (Figure 8), the dimer is characterised by a polar head that forms attractive hydrogen bonds and by a crowded organic tail with several short interactions, especially between hydrogen atoms, whose large repulsive contribution offsets the attractive contacts.

2) Despite the less favourable values of E_{es} with respect to pair A, pairs B and C show larger total attractive energies, 18 and 20 kJ mol^{-1}, respectively. This is due to the reduction in the repulsive term E_{rep}, which decreases to 38 and 13% (for B and C, respectively) of the value of

Table 8. Comparison between values of the total intermolecular interaction energies for six molecular pairs of **1**, as evaluated by different methods.

Pair[a]	d_{CM} [Å][b]	E_{int} [kJ mol^{-1}]		
		Experimental[c]	MCG-BLYP[d]	MCG-B3LYP[e]
A	6.037	$-10(3)$	12	-8
B	9.443	$-18(2)$	27	17
C	11.356	$-20(4)$	5	0
D	13.365	$-12(2)$	-2	-4
E	12.312	18(2)	18	13
F	12.389	2(2)	20	12

[a] Symmetry operations as in Table 7. [b] Distance between the centres of mass of the molecules in a pair. [c] Interaction energy obtained through Equation (12) (see text) applied to the experimental $\rho(\boldsymbol{r})$. The s.u. of the E_{es} term is given in parentheses. [d] Interaction energy, corrected for BSSE by the counterpoise method, obtained from MCG-BLYP calculations on the isolated dimers with the Morokuma–Ziegler decomposition scheme implemented in the ADF program. [e] Interaction energy, corrected for BSSE by the counterpoise method, obtained from MCG-B3LYP calculations on the isolated dimers through Equation (10) (see text).

dimer A, because of the increased distance between the centres of mass. Moreover, pair B is significantly stabilised by the large contribution of the dispersive term E_{disp}, attractive by 83 kJ mol^{-1}, which reflects a structural pattern in which the area of overlap between the atoms of the two subsystems is maximised[18] (Figure 8).

3) The E_{int} values from Equation (10) and Equation (11) for isolated dimers predict the same relative order of stability, with the exception of dimer A, which is calculated to be repulsive by the ADF program.[25, 26]

4) Conversely, the discrepancies between the estimates obtained for the crystal (third column) and those obtained for isolated dimers (fourth and fifth column) are large and call for further investigation. They have to be partly imputed to matrix effects: indeed, as the gas-phase dimers are treated as if they had the crystal geometry without previous optimisation it is not surprising that they are energetically less favoured than the in-crystal molecular pairs. Furthermore, some improvement could be achieved with a better estimate of the BSSE, whose correction by the counterpoise method is probably overestimated.[79] Finally, regarding the experimental estimate of E_{int} from Equation (12), it has been acknowledged[78] that the incorporation of the promolecular energies into the electrostatic term would necessitate redetermination of other terms in the force fields, especially the repulsion terms, and the achievement of this point, currently under investigation, would imply the determination of more realistic experimental interaction energies.

Conclusion

The structural, topological and electrostatic features of the antihypertensive drug milfasartan have been discussed from

the viewpoint of molecular recognition based on the assumption that the physical properties of a drug molecule in its crystal state, explaining the molecular self-affinity that gives rise to crystallisation, can rightly be used as the structural basis for recognising attractive interactions between the drug and its receptor. We have shown that electrostatic properties (derived from both the experimental electron density and the ab initio wavefunction) can be used, in addition to the usual structural parameters, as molecular descriptors of the binding affinity between the drug and its receptor and allow us to gain an insight into the physical nature of the drug–receptor interactions. In particular, the following conclusions can be drawn:

1) We have found, by means of QTAIM group charges, that milfasartan has a nearly spherical electron density distribution, characterised by a combination of electropositive and electronegative zones rather than by a unique electrophilic region opposed to a nucleophilic area.

2) As a consequence, odd-rank moments are scarcely significant and are ill-determined, whereas even-rank moments are large and significant.

3) Hydrogen bonding, accounting for up to 80% of the electrostatic interaction energy, effectively plays a key role in regulating the activity of sartan drugs and may be considered a meaningful driving force for the recognition process. The key pharmacophoric features of the hydrogen bonds are the acidic N6−HN6 group, the C12 and C11 methyl residues, the C5 methylene and two CH bonds of the aromatic rings as donors, and all five $N(sp^2)$ nitrogen atoms together with the sulfur and the three oxygen atoms as acceptors.

4) Dispersive interactions are important at the thiophene and at both the phenyl fragments, even if evidence of an electrostatic interaction between the o-phenyl ring and another aromatic ring has also been shown, when their mutual orientation is edge-to-face.

5) The new model proposed by Spackman to evaluate the electrostatic contribution to the intermolecular interaction energy has been successfully applied to an experimental charge density distribution of a large system (70 atoms) and appears to be a very powerful tool for the study of hydrogen-bonded crystals.

Most of the available literature on the relevance of first and second electrostatic moments in predicting the mechanism of reactivity in molecular recognition processes relates to the theoretical estimates of the mentioned quantities: we think that our work represents an important step in the direction of the experimental determination of the electrostatic properties, which may also become important in molecular mechanics calculations. The interplay between experiment and theory in this field can reveal further insights, such as the structural and electric rearrangements that occur upon crystallisation.

In terms of drug design, all the described pharmacophoric features must be taken into account in the further development of non-peptide AII receptor antagonists, which could potentially be improved by properly introducing stronger hydrogen-bond donor and acceptor groups. This study is therefore a useful guide to the rational development of highly effective sartan drugs.

Acknowledgements

[1] a) E. M. Krovat, T. Langer, *J. Med. Chem.* **2003**, *46*, 716–726; b) A. Kurup, R. Garg, D. J. Carini, C. Hansch, *Chem. Rev.* **2001**, *101*, 2727–2750; c) T. Mavromoustakos, A. Kolocouris, M. Zervou, P. Roumelioti, J. Matsoukas, R. Weisemann, *J. Med. Chem.* **1999**, *42*, 1714–1722; d) H. Yanagisawa, Y. Amemiya, T. Kanazaki, Y. Shimiji, K. Fujimoto, Y. Kitahara, T. Sada, M. Mizuno, M. Ikeda, S. Miyamoto, Y. Furukawa, H. Koike, *J. Med. Chem.* **1996**, *39*, 323–338; e) R. R. Wexler, W. J. Greenlee, J. D. Irvin, M. R. Goldberg, K. Prendergast, R. D. Smith, P. B. M. W. M. Timmermans, *J. Med. Chem.* **1996**, *39*, 625–656.

[2] G. Berellini, G. Cruciani, R. Mannhold, *J. Med. Chem.* **2005**, *48*, 4389–4399.

[3] A. Salimbeni, R. Canevotti, F. Paleari, D. Poma, S. Caliari, F. Fici, R. Cirillo, A. R. Renzetti, A. Subissi, L. Belvisi, G. Bravi, C. Scolastico, A. Giachetti, *J. Med. Chem.* **1995**, *38*, 4806–4820.

[4] B. C. Wilkes, L. Masaro, P. W. Schiller, K. A. Carpenter, *J. Med. Chem.* **2002**, *45*, 4410–4418.

[5] E. D. Stevens, C. L. Klein, *Trans. Am. Crystallogr. Assoc.* **1990**, *26*, 79–89.

[6] a) A. D. Buckingham in *Physical Chemistry. An Advanced Treatise* (Ed.: D. Henderson), Academic Press, New York, **1970**, pp. 349–386; b) A. D. Buckingham in *Intermolecular Interactions: From Diatomics to Biopolymers* (Ed.: B. Pullmann), Wiley, Chichester, New York, **1978**, pp. 1–67.

[7] A. J. Stone, *The Theory of Intermolecular Forces*, International Series of Monographs in Chemistry, Clarendon Press, Oxford, **1996**.

[8] P. Politzer, J. S. Murray, Z. Peralta-Inga, *Int. J. Quantum Chem.* **2001**, *85*, 676–684.

[9] T. S. Koritsanszky, P. Coppens, *Chem. Rev.* **2001**, *101*, 1583–1627.

[10] S. Ahmad, A. Sarai, *J. Mol. Biol.* **2004**, *341*, 65–71.

[11] a) J. R. Trudell, *Biophys. Chem.* **1998**, *73*, 7–11; b) N. Bouhmaida, M. Dutheil, N. E. Ghermani, P. Becker, *J. Chem. Phys.* **2002**, *116*, 6196–6204.

[12] a) S. Hirokawa, T. Imasaka, T. Imasaka, *Chem. Res. Toxicol.* **2005**, *18*, 232–238; b) B. J. Mhin, J. E. Lee, W. Choi, *J. Am. Chem. Soc.* **2002**, *124*, 144–148.

[13] E. M. Burgess, J. A. Ruell, L. H. Zalkow, *J. Med. Chem.* **1995**, *38*, 1635–1640.

[14] a) M. A. Spackman, *Chem. Rev.* **1992**, *92*, 1769–1797; b) M. A. Spackman, A. S. Brown, *Annu. Rep. Prog. Chem., Sect. C* **1994**, *91*, 175–212; c) M. A. Spackman, *Annu. Rep. Prog. Chem., Sect. C* **1998**, *94*, 177–207.

[15] R. Destro, R. Soave, M. Barzaghi, L. Lo Presti, *Chem. Eur. J.* **2005**, *11*, 4621–4634.

[16] The AII receptors belong to the 7TM superfamily of G-protein-coupled receptors and are divided into two subtypes, AT_1 and AT_2. Of the 7TM superfamily of receptors, only bovine rhodopsin has been structurally characterised (K. Palczewski, T. Kumasaka, T. Hori, C. A. Behnke, H. Motoshima, B. A. Fox, I. Le Trong, D. C. Teller, T. Okada, R. E. Stenkamp, M. Yamamoto, M. Miyano, *Science* **2000**, *289*, 739–745), whereas all the others are at the present time intractable to study by crystallography. For more details on AII receptors

see: C. D. Strader, T. M. Fong, M. R. Tota, D. Underwood, R. A. Dixon, *Annu. Rev. Biochem.* **1994**, *63*, 101–132.

[17] J. D. Dunitz, A. Gavezzotti, *Angew. Chem.* **2005**, *117*, 1796–1819; *Angew. Chem. Int. Ed.* **2005**, *44*, 1766–1787.

[18] E. A. Meyer, R. K. Castellano, F. Diederich, *Angew. Chem.* **2003**, *115*, 1244–1287; *Angew. Chem. Int. Ed.* **2003**, *42*, 1210–1250.

[19] R. F. W. Bader, *Atoms in Molecules: A Quantum Theory*, Oxford University Press, Oxford, **1990**.

[20] In terms of least-squares refinement correlation coefficients, the size of our data set $[(\sin\theta/\lambda)_{max} = 0.86\ \text{Å}^{-1}]$ at 17 K is equivalent to a data set up to $(\sin\theta/\lambda)_{max} = 1.1\ \text{Å}^{-1}$ at 120 K (see ref. [21b]).

[21] a) R. F. Stewart, *J. Chem. Phys.* **1969**, *51*, 4569–4577; b) R. F. Stewart, *Acta Crystallogr., Sect. A* **1976**, *32*, 565–574; c) R. F. Stewart in *The Applications of Charge Density Research to Chemistry and Drug Design* (Eds.: G. A. Jeffrey, J. F. Piniella), Plenum Press, New York, **1991**, pp. 63–101.

[22] P. Roversi, R. Destro, *Chem. Phys. Lett.* **2004**, *386*, 472–478.

[23] R. F. Stewart, M. A. Spackman, C. Flensburg, *VALRAY User's Manual (Version 2.1)*, Carnegie-Mellon University, Pittsburg, and University of Copenhagen, Copenhagen, **2000**.

[24] Gaussian 98, Revision A.11.3, M. J. Frisch, G. W. Trucks, H. B. Schlegel, G. E. Scuseria, M. A. Robb, J. R. Cheeseman, V. G. Zakrzewski, J. A. Montgomery, Jr., R. E. Stratmann, J. C. Burant, S. Dapprich, J. M. Millam, A. D. Daniels, K. N. Kudin, M. C. Strain, O. Farkas, J. Tomasi, V. Barone, M. Cossi, R. Cammi, B. Mennucci, C. Pomelli, C. Adamo, S. Clifford, J. Ochterski, G. A. Petersson, P. Y. Ayala, Q. Cui, K. Morokuma, N. Rega, P. Salvador, J. J. Dannenberg, D. K. Malick, A. D. Rabuck, K. Raghavachari, J. B. Foresman, J. Cioslowski, J. V. Ortiz, A. G. Baboul, B. B. Stefanov, G. Liu, A. Liashenko, P. Piskorz, I. Komaromi, R. Gomperts, R. L. Martin, D. J. Fox, T. Keith, M. A. Al-Laham, C. Y. Peng, A. Nanayakkara, M. Challacombe, P. M. W. Gill, B. Johnson, W. Chen, M. W. Wong, J. L. Andres, C. Gonzalez, M. Head-Gordon, E. S. Replogle, J. A. Pople, Gaussian, Inc., Pittsburgh, PA, **2002**.

[25] G. te Velde, F. M. Bickelhaupt, S. J. A. van Gisbergen, C. Fonseca Guerra, E. J. Baerends, J. G. Snijders, T. Ziegler, *J. Comput. Chem.* **2001**, *22*, 931–967.

[26] ADF2004.01, SCM, E. J. Baerends, J. Autschbach, A. Bérces, C. Bo, P. M. Boerrigter, L. Cavallo, D. P. Chong, L. Deng, R. M. Dickson, D. E. Ellis, L. Fan, T. H. Fischer, C. Fonseca Guerra, S. J. A. van Gisbergen, J. A. Groeneveld, O. V. Gritsenko, M. Grüning, F. E. Harris, P. van den Hoek, H. Jacobsen, G. van Kessel, F. Kootstra, E. van Lenthe, D. A. McCormack, V. P. Osinga, S. Patchkovskii, P. H. T. Philipsen, D. Post, C. C. Pye, W. Ravenek, P. Ros, P. R. T. Schipper, G. Schreckenbach, J. G. Snijders, M. Sola, M. Swart, D. Swerhone, G. te Velde, P. Vernooijs, L. Versluis, O. Visser, E. van Wezenbeek, G. Wiesenekker, S. K. Wolff, T. K. Woo, T. Ziegler, Theoretical Chemistry, Vrije Universiteit, Amsterdam (http://www.scm.com).

[27] A. D. Becke, *J. Chem. Phys.* **1993**, *98*, 5648–5652.

[28] C. Lee, W. Yang, R. G. Parr, *Phys. Rev. B* **1988**, *37*, 785–789.

[29] A. D. Becke, *Phys. Rev. A* **1988**, *38*, 3098–3100.

[30] V. R. Saunders, R. Dovesi, C. Roetti, R. Orlando, C. M. Zicovich-Wilson, N. M. Harrison, K. Doll, B. Civalleri, I. Bush, Ph. D'Arco, M. Llunell, *CRYSTAL2003 User's Manual*, University of Torino, Torino, **2003**.

[31] In order to avoid numerical instabilities in the calculation with the standard split-valence basis set, the diffuse outermost Gaussian function of all atoms was modified: the exponent was set to $^4/_3$ of its standard value.

[32] S. F. Boys, F. Bernardi, *Mol. Phys.* **1970**, *19*, 553–566.

[33] M. Barzaghi, *PAMoC (Version 2005.0), Online User's Manual*, CNR-ISTM, Institute of Molecular Science and Technologies, Milano, **2005** (http://www.istm.cnr.it/pamoc/).

[34] a) F. W. Biegler-König, R. F. W. Bader, T.-H. Tang, *J. Comput. Chem.* **1982**, *3*, 317–328; b) AIMPAC download page: http://www.chemistry.mcmaster.ca/aimpac.

[35] V. Bertolasi, P. Gilli, V. Ferretti, G. Gilli, *Acta Crystallogr., Sect. B* **2001**, *57*, 591–598.

[36] a) B. M. Goldstein, F. Takusagawa, H. M. Berman, P. C. Srivastava, R. K. Robins, *J. Am. Chem. Soc.* **1983**, *105*, 7416–7422; b) P. Franchetti, L. Cappellacci, M. Grifantini, A. Barzi, G. Nocentini, H. Yang, A. O'Connor, H. N. Jayaram, C. Carrell, B. M. Goldstein, *J. Med. Chem.* **1995**, *38*, 3829–3837; c) H. Li, W. A. Hallows, J. S. Punzi, V. E. Marquez, H. L. Carrell, K. W. Pankiewicz, K. A. Watanabe, B. M. Goldstein, *Biochemistry* **1994**, *33*, 23–32.

[37] Y. Nagao, T. Hirata, S. Goto, S. Sano, A. Kakehi, K. Iizuka, M. Shiro, *J. Am. Chem. Soc.* **1998**, *120*, 3104–3110.

[38] G. J. Moore, R. C. Ganter, J. M. Matsoukas, J. Hondrelis, G. Agelis, K. Barlos, S. Wilkinson, J. Sandall, P. Fowler, *J. Mol. Recognit.* **1994**, *7*, 251–256.

[39] J. M. Matsoukas, L. Polevaya, J. Ancans, T. Mavromoustakos, A. Kolocouris, P. Roumelioti, D. V. Vlahakos, R. Yamdagni, Q. Wu, G. J. Moore, *Bioorg. Med. Chem.* **2000**, *8*, 1–10.

[40] a) A. Paturle, P. Coppens, *Acta Crystallogr., Sect. A* **1988**, *44*, 6–7; b) P. Coppens, *X-Ray Charge Densities and Chemical Bonding*, Oxford University Press, New York, **1997**.

[41] QTAIM performs a topological analysis of $\rho(\boldsymbol{r})$ and divides all space into non-overlapping regions separated by surfaces on which $\nabla\rho(\boldsymbol{r})\boldsymbol{n}$ is zero, where $\boldsymbol{n}$ is a vector normal to the surfaces.

[42] X. Li, G. Wu, Y. A. Abramov, A. V. Volkov, P. Coppens, *Proc. Nat. Am. Soc. (USA)* **2002**, *99*, 12132–12137.

[43] A. D. McLean, M. Yoshimine, *J. Chem. Phys.* **1967**, *47*, 1927–1935.

[44] The precision of the moments obtained can be estimated by comparison with those evaluated through the standard theoretical procedure. Differences were in any case less than 2% for $|\boldsymbol{m}^{(1)}|$ and 0.1% for Tr $\boldsymbol{m}^{(2)}$.

[45] R. S. Mulliken, *J. Chem. Phys.* **1955**, *23*, 1833–1840.

[46] A. E. Whitten, C. J. Radford, J. J. McKinnon, M. A. Spackman, *J. Chem. Phys.* **2006**, *124*, 074106 (1–9).

[47] A. E. Whitten, P. Turner, W. T. Klooster, R. O. Piltz, M. A. Spackman, *J. Phys. Chem. A* **2006**, *110*, 8763–8776.

[48] E. May, R. Destro, C. Gatti, *J. Am. Chem. Soc.* **2001**, *123*, 12248–12254.

[49] XD-Computer program package for multipole refinement and topological analysis of electron densities from diffraction data, T. Koritsanszky, T. Richter, P. Macchi, A. Volkov, C. Gatti, S. Howard, P. R. Mallinson, L. Farrugia, Z. Su, N. K. Hansen, **2003**.

[50] M. Barzaghi, R. Soave, R. Destro, unpublished results.

[51] M. A. Spackman, P. G. Byrom, *Acta Crystallogr., Sect. B* **1996**, *52*, 1023–1035.

[52] H.-B. Bürgi, S. C. Capelli, A. E. Goeta, J. A. K. Howard, M. A. Spackman, D. S. Yufit, *Chem. Eur. J.* **2002**, *8*, 3512–3521.

[53] A. Forni, R. Destro, *Chem. Eur. J.* **2003**, *9*, 5528–5537.

[54] S. Pérez-Casas, J. Hernández-Trujillo, M. Costas, *J. Phys. Chem. B* **2003**, *107*, 4167–4174.

[55] a) A. Baumgärtner, *J. Chem. Phys.* **1993**, *98*, 7496–7501; b) J. J. McKinnon, A. S. Mitchell, M. A. Spackman, *Chem. Eur. J.* **1998**, *4*, 2136–2141.

[56] For spherical shapes $(\Lambda_X \approx \Lambda_Y \approx \Lambda_Z)$ $A = 0$, for oblate shapes $(\Lambda_X < \Lambda_Y \approx \Lambda_Z)$ $A = ^1/_2$ and for prolate shapes $(\Lambda_X \approx \Lambda_Y < \Lambda_Z)$ $A = 1$.

[57] S. P. Kampermann, J. R. Ruble, B. M. Craven, *Acta Crystallogr. Sect. B* **1994**, *50*, 737–741.

[58] A. Fkyerat, A. Guelzim, F. Baert, J. Zyss, A Périgaud, *Phys. Rev. B* **1996**, *53*, 16236–16246.

[59] A. Chouaih, F. Hamzaoui, G. Vergoten, *J. Mol. Struct.* **2005**, *738*, 33–38.

[60] R. Bianchi, A. Forni, *J. Appl. Crystallogr.* **2005**, *38*, 232–236.

[61] P-B3LYP values for third and fourth moments are not available because CRYSTAL2003 provides only a Mulliken DMA in the form of spherical harmonic tensors.

[62] U. Koch, P. L. A. Popelier, *J. Phys. Chem.* **1995**, *99*, 9747–9754.

[63] Y. A. Abramov, A. Volkov, G. Wu, P. Coppens, *J. Phys. Chem. B* **2000**, *104*, 2183–2188.

[64] Y. A. Abramov, *Acta Crystallogr., Sect. A* **1997**, *53*, 264–272.

[65] E. Espinosa, E. Molins, C. Lecomte, *Chem. Phys. Lett.* **1998**, *285*, 170–173.

[66] It has been noted (C. Gatti, E. May, R. Destro, F. Cargnoni, *J. Phys. Chem. A* **2002**, *106*, 2707–2720) that Equation (9) may fail when applied to weak CH⋯O interactions and new relationships have been proposed. On the other hand, these relationships were found to underestimate the energies of strong hydrogen bonds such as OH⋯O interactions in the fungal metabolite austdiol (L. Lo Presti, R. Soave, R. Destro, *J. Phys. Chem. B* **2006**, *110*, 6405–6414].

[67] E. A. Zhurova, A. Martin, A. A. Pinkerton, *J. Am. Chem. Soc.* **2002**, *124*, 8741–8750.

[68] Equation (9) converts a local density property ($V(r)_{bcp}$) into a relative energy scale. We believe that the potential energy density at an H⋯Y bond critical point is a more valuable descriptor of the strength of this type of bond, but for the general chemistry community a bond strength is better expressed in terms of energy.

[69] P. Coppens, Y. A. Abramov, M. Carducci, B. Korjov, I. Novozhilova, C. Alhambra, M. R. Pressprich, *J. Am. Chem. Soc.* **1999**, *121*, 2585–2593.

[70] R. Soave, R. Destro, M. Barzaghi, unpublished results.

[71] Y. Gu, T. Kar, S. Scheiner, *J. Am. Chem. Soc.* **1999**, *121*, 9411–9422.

[72] R. Cini, C. Bellucci, G. Tamasi, M. Corsini, M. Fontani, P. Zanello, *Inorg. Chim. Acta* **2002**, *339*, 89–103.

[73] S. Scheiner, T. Kar, J. Pattanayak, *J. Am. Chem. Soc.* **2002**, *124*, 13257–13264.

[74] T. Ziegler, A. Rauk, *Theor. Chim. Acta* **1977**, *46*, 1–10.

[75] K. Morokuma, *J. Chem. Phys.* **1971**, *55*, 1236–1244.

[76] M. A. Spackman, H. P. Weber, B. M. Craven, *J. Am. Chem. Soc.* **1988**, *110*, 775–782.

[77] M. A. Spackman, *J. Phys. Chem.* **1987**, *91*, 3179–3186.

[78] M. A. Spackman, *Chem. Phys. Lett.* **2006**, *418*, 158–162.

[79] J. J. Novoa, M. Planas, M.-H. Whangbo, *Chem. Phys. Lett.* **1994**, *225*, 240–246.